University of Kent

Kent Academic Repository

Tang, Hujun, Sun, Feifei, Shen, Tao, Feng, Yue, Liu, Chi, Liu, Xin and Wang, Chao (2024) *Photonic crystal fiber sensors to excite surface plasmon resonance based on elliptical detection channels are used for highly sensitive magnetic sensing.* Journal of the Optical Society of America B, 41 (4). pp. 998-1007. ISSN 0740-3224.

Downloaded from

https://kar.kent.ac.uk/114471/ The University of Kent's Academic Repository KAR

The version of record is available from

https://doi.org/10.1364/JOSAB.506522

This document version

Publisher pdf

DOI for this version

Licence for this version

CC BY (Attribution)

Additional information

Versions of research works

Versions of Record

If this version is the version of record, it is the same as the published version available on the publisher's web site. Cite as the published version.

Author Accepted Manuscripts

If this document is identified as the Author Accepted Manuscript it is the version after peer review but before type setting, copy editing or publisher branding. Cite as Surname, Initial. (Year) 'Title of article'. To be published in ***Title of Journal*** , Volume and issue numbers [peer-reviewed accepted version]. Available at: DOI or URL (Accessed: date).

Enquiries

If you have questions about this document contact ResearchSupport@kent.ac.uk. Please include the URL of the record in KAR. If you believe that your, or a third party's rights have been compromised through this document please see our Take Down policy (available from https://www.kent.ac.uk/guides/kar-the-kent-academic-repository#policies).

Journal of the Optical Society of America B
OPTICAL PHYSICS

Photonic crystal fiber sensors to excite surface plasmon resonance based on elliptical detection channels are used for highly sensitive magnetic sensing

HUJUN TANG,[1] FEIFEI SUN,[1,*] TAO SHEN,[1,2] YUE FENG,[2] CHI LIU,[1,3] XIN LIU,[1] AND CHAO WANG[4]

[1]Heilongjiang Province Key Laboratory of Laser Spectroscopy Technology and Application, Harbin University of Science and Technology, Harbin 150080, China
[2]Key Laboratory of Engineering Dielectrics and Its Application, Ministry of Education, Harbin University of Science and Technology, Harbin, 150080, China
[3]School of Computer Science and Technology, Harbin University of Science and Technology, Harbin, 150080, China
[4]School of Engineering, University of Kent, Canterbury, UK
*928941089@qq.com

Received 21 September 2023; revised 1 February 2024; accepted 3 February 2024; posted 8 February 2024; published 19 March 2024

To improve the detection performance of fiber optic magnetic field sensors a new photonic crystal fiber (PCF) based on surface plasmon resonance (SPR) was designed and investigated. The designed sensor uses an elliptical detection channel, and the modal transmission characteristics and magnetic field sensing characteristics of this fiber optic sensor are analyzed using the full vector finite element method (FVFEM). In addition, the effect of the detection channel on the detection accuracy at different curvatures was investigated. Compared with previous optical fiber magnetic field (MF) sensors, the designed sensor meets the requirements of both refractive index (RI) and MF measurements, and the MF sensitivity, RI sensitivity, and amplitude sensitivity (AS) of the sensor reach 0.739 nm/Oe, 12043.8 nm/RIU, and 754.88 RIU^{-1}, respectively. The designed sensor expands the application range of optical fiber sensors and reduces the cost. It has great potential for application in complex environments. © 2024 Optica Publishing Group

https://doi.org/10.1364/JOSAB.506522

1. INTRODUCTION

Magnetic field (MF) is an important basic parameter. MF measurement plays an increasingly important role in many fields such as power system monitoring, navigation, earthquake warning, radio communication, medical treatment, military, and so on [1]. Electromagnetic field sensors have been extensively studied and applied in practice earlier [2]. In 2019, Nakamura *et al*. developed a MF sensor that can measure magnetic flux density and the localization of measurement points in space in a very short time [3]. In 2020, Cavaliere *et al*. proposed a repeatable sensor for the optimization and implementation of air-core and ferrite-core inductive sensors suitable for AC-based electromagnetic tracking, which has a static tracking error of less than 2 mm [4]. However, the above electromagnetic field sensors have the disadvantages of large size, high cost, poor environmental adaptability, and limited test dynamic range [5]. Therefore, improving the measurement accuracy is an urgent problem to be solved [6].

Photonic crystal fiber (PCF) has received widespread attention for its outstanding advantages such as high integration, high birefringence, high sensitivity, and outstanding resistance to electromagnetic interference, and has been regarded as an effective way to solve these problems [7]. Surface plasmon resonance (SPR) is a physical phenomenon in which light propagating through an optical fiber achieves a total reflection effect, at which point the light generates an exponentially dissipating wave on the surface of the metal film, known as a swift wave. The free electrons on the surface of the metal form a surface plasma wave (SPW) that resonates when some of the two wave bands meet [8,9]. The surface plasmon polariton (SPP) mode has a strong electromagnetic field, which is sensitive to small changes in the RI of the analyte. Therefore, SPR technology is used to achieve physical parameter sensing widely [10]. PCF with the combination of SPR in measuring the RI, MF, temperature, and stress has great potential. In 2021, Xie *et al.* studied in detail the method to improve the sensitivity and linearity based on a conventional PCF-SPR with a hexagonal air

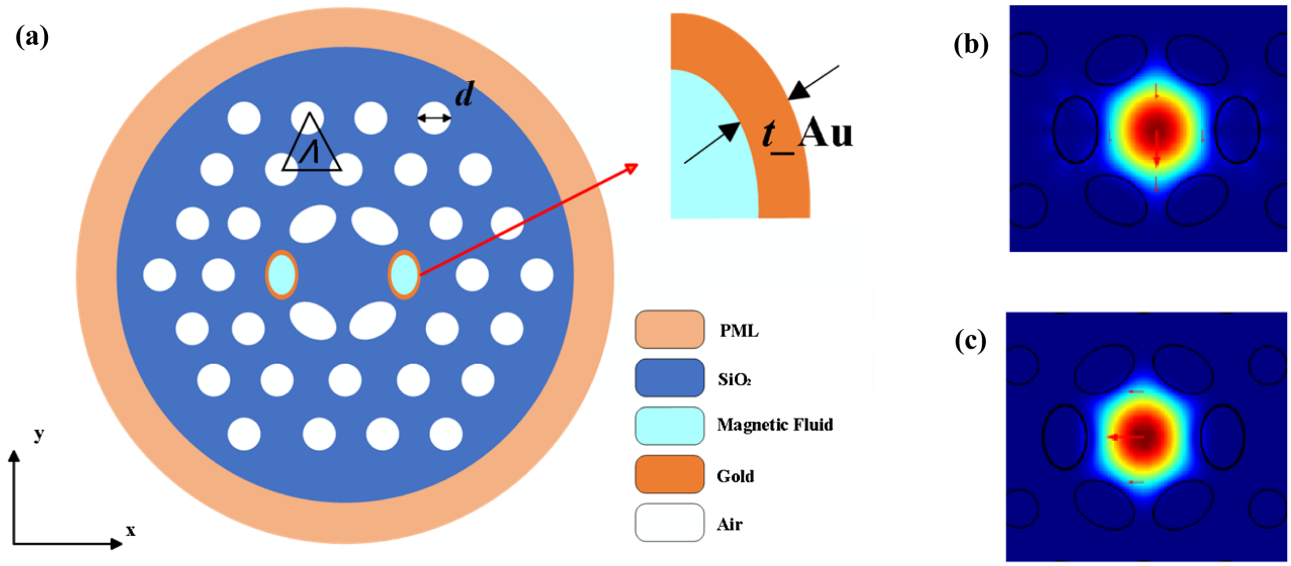


Fig. 1. (a) Cross section of the PCF-SPR sensor; (b) electric field distribution of the Y-Pol fundamental mode at 650 nm; (c) electric field distribution of the X-Pol fundamental mode at 650 nm.

hole arrangement, with a RI detection range of 1.15–1.45. The wavelength sensitivity of it is up to 5893.9 nm/RIU [11].

The MF sensing principle of the PCF-SPR sensor is to use the guided wave in the fiber core to couple to the MF through the outgoing field and use the magnetic response characteristics of the magnetic field to realize the optical field modulation and MF sensing. The main characteristics of magnetic fluids used in sensors are their unique superparamagnetic and good fluidity, that is, the response speed and volume change speed in the magnetic field are fast [12]. Magnetic field sensing is designed by combining magnetic refractive modulation of magnetic fluids with optics of different structures [13,14]. In 2019, Liu *et al.* designed a dual-core PCF optic sensor that simultaneously measures MF and temperature based on SPR. The sensor's MF sensitivity can reach 0.44 nm/mT [15]. In 2019, Wang *et al.* designed a high-sensitivity MF sensor based on dual-core PCF. The sensor sensitivity is up to 442.7 pm/Oe [16].

The elliptical channel PCF-SPR sensor using the magnetic refraction effect proposed in this paper is proposed. The fully vectorial finite element method (FVFEM) analyzed its sensing mode characteristics and MF characteristics. The sensor structure consists of an outer hexagonal arrangement of circular pores and an inner elliptical channel. Two elliptical channels symmetrical to the core are filled with material. This selective filling structure reduces the absorption loss in the material and improves the coupling efficiency between the surface plasma and the core mode [17], further reducing costs. There is enormous potential for environmental magnetic anomalies and medical diagnostics.

2. MODEL AND THEORY

Figure 1(a) shows a two-dimensional cross section of the designed sensor. The sensor consists of two small air holes and elliptical channels surrounding the core. The elliptical channels on the left and right sides of the core are filled with magnetic fluid and a layer of metallic gold is plated on the outermost periphery to excite SPR. A perfectly matched layer (PML) is added to the outermost layer of the PCF along with scattering boundary conditions for absorbing radiant energy from surfaces. In terms of structural parameters, the diameter of the small air holes is d, the spacing is Λ, the distance between the elliptical air holes and $t_{_Au}$ is the thickness of the gold layer, a represents the horizontal axis of the oval channel, and b represents the vertical axis of the oval channel. The electric field diagram of the designed PCF structure is shown in Figs. 1(b) and 1(c). From the figure, the energy is mainly concentrated in the central region, and the polarization can be classified into X-Pol and Y-Pol according to the direction of the electric field. Figures 1(b) and 1(c) show the electric field distribution for both polarizations at a wavelength of 650 nm. The red arrows indicate the direction of polarization of the electric field. In the simulation, the initial setup parameters are shown in Table 1.

Table 1. Initial Setting Parameters Setting

Reference	Parameter	Value
Λ	The pitch of air hole	4 μm
d	The diameter of the air holes	2 μm
$t_{_Au}$	The thickness of the gold film	35 nm
a	The horizontal axis of the oval channel	2 μm
b	The vertical axis of the oval channel	3 μm

The cladding material used for the designed structure is SiO_2, and its dispersion formula can be expressed by the Sellmeier equation [18]:

$$n^2(\lambda) = 1 + \frac{A_1\lambda^2}{\lambda^2 - C_1} + \frac{A_2\lambda^2}{\lambda^2 - C_2} + \frac{A_3\lambda^2}{\lambda^2 - C_3}. \quad (1)$$

According to the above formula, n denotes the RI of SiO_2, λ denotes the wavelength of the incident light, and the remainder are all constant values, and the rest of the constants are $A_1 = 0.696166300$, $A_2 = 0.407942600$, $A_3 = 0.897479400$,

$C_1 = 0.0046791482\ \mu m$, $C_2 = 0.0135120631\ \mu m$, and $C_3 = 97.9340025\ \mu m$.

The RI of the magnetic fluid with the external MF can be described by the Langevin function [19]:

$$n_{MF} = (n_s - n_0)\left[\coth\left(\alpha\frac{H - H_{c,n}}{T}\right) - \frac{T}{\alpha(H - H_{c,n})}\right] + n_0, \quad H > H_{c,n}, \tag{2}$$

where n_{MF} denotes the RI of the magnetic fluid, n_s denotes the saturation RI of the magnetic fluid, and n_0 is the initial RI of the magnetic fluid, which is determined by the concentration of the magnetic fluid. n_s is set to 1.42318, and n_0 is set to 1.4352. H and $H_{c,n}$ denote the external MF and the MF threshold, respectively, where $H_{c,n}$ is set to 20 Oe. $T = 20.0°C$ is the ambient temperature and $\alpha = 5$ is the fitting coefficient.

The dielectric constant of gold can be expressed using the Drude–Lorentz model [20]:

$$\varepsilon_{Au} = \varepsilon_\infty - \frac{\omega_D^2}{\omega(\omega + j\gamma_D)} - \frac{\Delta\varepsilon \cdot \Omega_L^2}{(\omega^2 - \Omega_L^2) + j\Gamma_L\omega}, \tag{3}$$

where ε_{Au} denotes the gold dielectric constant and ε_∞ denotes the high-frequency dielectric constant. The value of the weighting factor is $\Delta\varepsilon$, ω denotes the angular frequency, and ω_D and γ_D are the plasma frequency and damping frequency, respectively. ω_L is the oscillator strength and Γ_L is the spectral width.

The relationship between the confinement loss and the RI of the core mode is given by the following equation [21]:

$$L = 8.686 \times \frac{2\pi}{\lambda}\mathrm{Im}[n_{\mathrm{eff}}] \times 10^4\left(\frac{dB}{cm}\right), \tag{4}$$

where Im[$n$eff] is the imaginary part of the effective RI.

3. ANALYSIS OF MODE CHARACTERISTICS

Figure 2(a) shows a three-dimensional model of the structure. The structure of the sensor is manufactured by stacking, stamping, and drilling during the manufacturing process [22]. The filling of magnetic fluids can be achieved by the method of pressure injection [23]. The specific experimental optical pathway is shown in Fig. 2(b). The incident light is emitted from the broadband light source and enters the sensing unit through the polarizer controller (PC), which energizes the Helmholtz coil with DC current to generate a MF from 20 to 100 Oe. Changes in the external MF cause changes in the sensing unit, resulting in a change in the spectrum, and finally the optical spectrum analyzer (OSA) displays the results of the changes, and the measurement of the MF is achieved based on the spectral changes.

Figure 3 shows the dispersion relationship between the X-Pol mode and the SPP mode when coupling occurs, and the loss curve between the X-Pol mode and the Y-Pol mode. The solid blue line denotes the constraint loss curve of the X-Pol core mode, the blue dashed line denotes the constraint loss curve of the Y-Pol mode, the solid red line denotes the effective RI real part of the X-Pol mode, and the solid black line denotes the effective RI real part of the SPP mode. We can see that the solid black line intersects the solid red line at 655 nm. At this moment, the effective RI real part of the core mode is equal to the effective RI real part of the SPP mode, and the phase matching condition is reached, so the SPR phenomenon is generated.

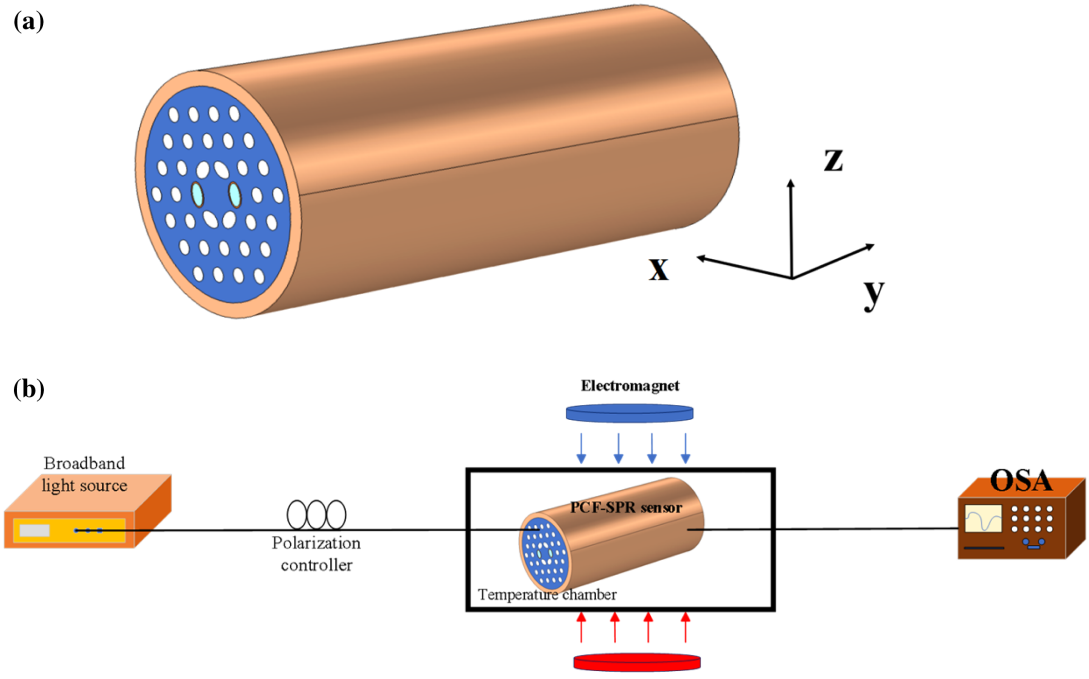


Fig. 2. (a) Schematic of the three-dimensional (3D) model of the sensor; (b) experimental device of the sensor.

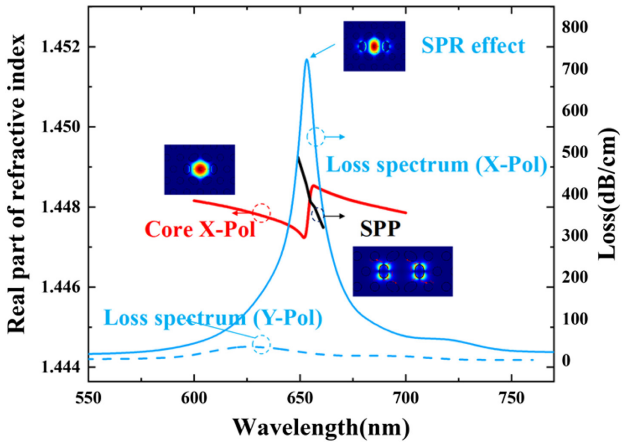


Fig. 3. Dispersion relationship between the X-Pol fiber and Y-Pol fiber core mode, SPP mode, and the loss spectrum of the PCF-SPR sensor.

At the same time, a loss peak is generated in the spectrum, and the magnetic field is measured by changing the position of the loss peak.

In addition, as we can see the coupling intensity in the X-Pol is much greater than the coupling intensity in the Y-Pol, which means that the core mode in the X-Pol can better excite SPR and has better sensing ability, so only the polarization in the X-Pol is studied in subsequent research discussions.

4. OPTIMIZATION OF STRUCTURAL PARAMETERS

The proposed sensor structural parameters, the long axes of the elliptical channel a, the short axes of the elliptical channel b, the air hole spacing Λ, the air hole diameter d, and the thickness of the metal layer $t_{_Au}$ were optimized, and the effect of the variation of the sensor structural parameters on the X-Pol constraints was investigated.

A. Influence of Sensing Channel Shape on Sensor Performance

We have discussed the horizontal and vertical axes of the elliptical channel, and we have set a to be the horizontal axis of the ellipse and b to be the vertical axis of the ellipse. Figures 4(a)–4(c) show the core mode electric field diagrams of X-Pol for $a > b$, $a = b$, and $a < b$, respectively. Figure 4(d) shows the loss curves of the X-Pol for the three channel modes. We can see that the peak of the loss curve is greatest when $a > b$. In this form, however, the change in resonance wavelength (RW) with RI is very insignificant and the wavelength drift is almost negligible. The sensing performance of the sensor in elliptical channels with different long and short axes is shown in Table 2. It can be easily seen that the sensing performance of the sensor is optimal when $a < b$. So, the proposed elliptical channel sensor has a better sensing effect compared to the circular channel.

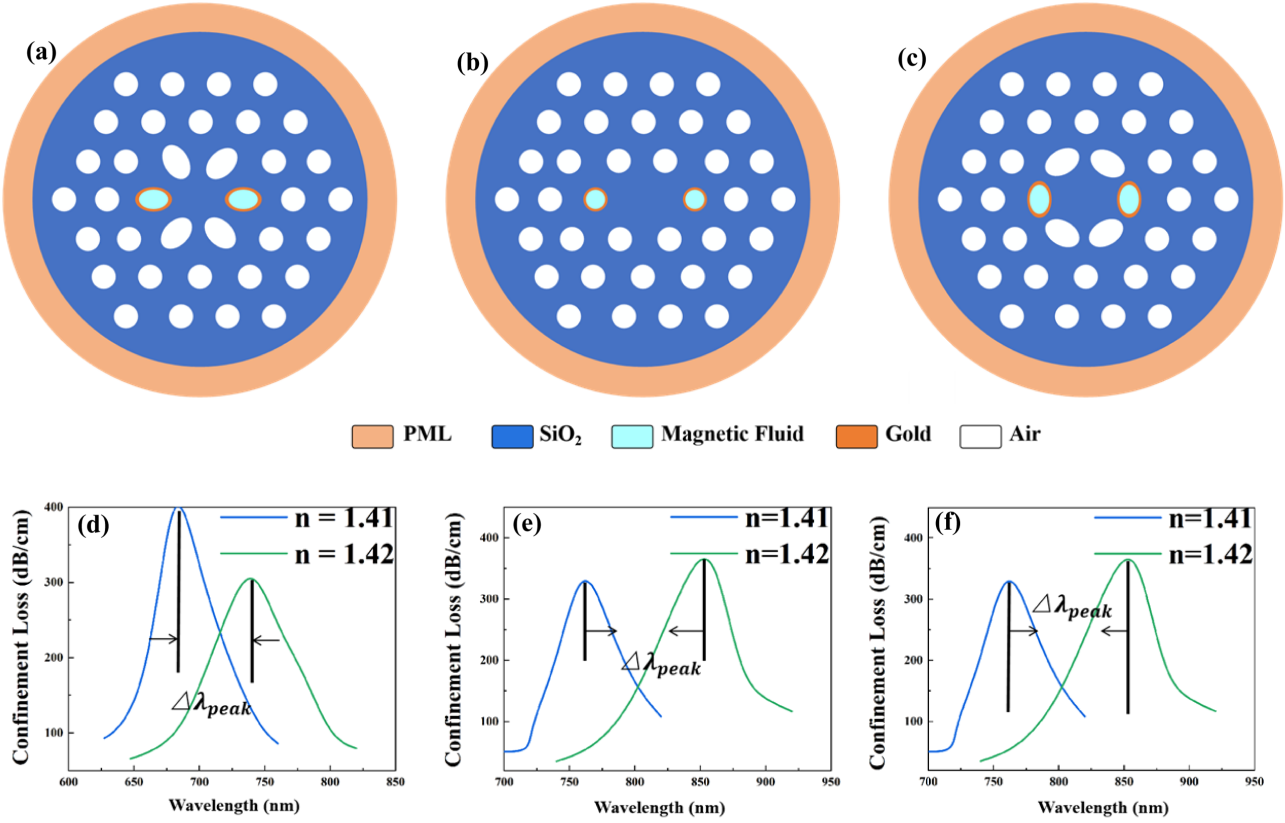


Fig. 4. Horizontal and vertical axes of elliptical channels. (a) $a > b$; (b) $a = b$; (c) $a < b$; (d) loss spectrum under different long and short axes; (e) wavelength shift when $a < b$; (f) wavelength shift when $a > b$.

Table 2. Sensing Performance of Sensors in Elliptical Channels with Different Long and Short Axes

	$\Delta\lambda_{peak}$ (nm)	Wave. Sens. S_λ (nm/RIU)	Amp. Sen. S_A (RIU^{-1})
$a > b$	50.37	5037	189.22
$a = b$	56.22	5622	605.55
$a < b$	120.44	12044	754.88

B. Pitch of Outer Air Holes

The effect of modifying the stomatal spacing on the sensor constraint loss for both refractive indices is illustrated in Fig. 5(a). From Figs. 5(b)–5(d), as Λ increases, the loss increases and then decreases, the resonant wavelength shifts slightly red, and the FWHM first decreases and then increases. This is mainly because the increase in Λ changes the effective RI of the core and SPP modes. In addition, the effective RI of the core mode changes more than that of the SPP mode as Λ increases, resulting in a red shift of the SPR phase matching point. In addition, when Λ is set to 3.9 μm, the SPP mode and the X-Pol core mode reach the optimal coupling point when the FWHM is the smallest, indicating that the detection effect is most obvious currently. Therefore, to improve the detection accuracy, a Λ of 3.9 μm is chosen in this paper.

C. Diameter of Air Holes

Figure 6 depicts the effect on the performance of the proposed sensor at different small air hole diameters. As the diameter of the air hole changes from 1.8 to 2.2 μm, the figure shows that a small change in the diameter of the outer hole has a very limited and almost negligible effect on the X-Pol limiting loss. Therefore, we keep the stomatal diameter at 2 μm in the following discussion.

D. Gold Film Thickness

Figure 7 explores the effect of t_{Au} on sensor performance. In the process of changing the t_{Au} from 32 to 36 nm, the peak value of the loss peak gradually increases, and the resonance wavelength is blue-shifted, among which the coupling strength is the largest when the thickness of the gold layer is 33 nm. As the t_{Au} increases, it is shown that the loss peak first increases and begins to decrease. Under the wavelength interrogation condition, the highest constraint loss is achieved when the gold

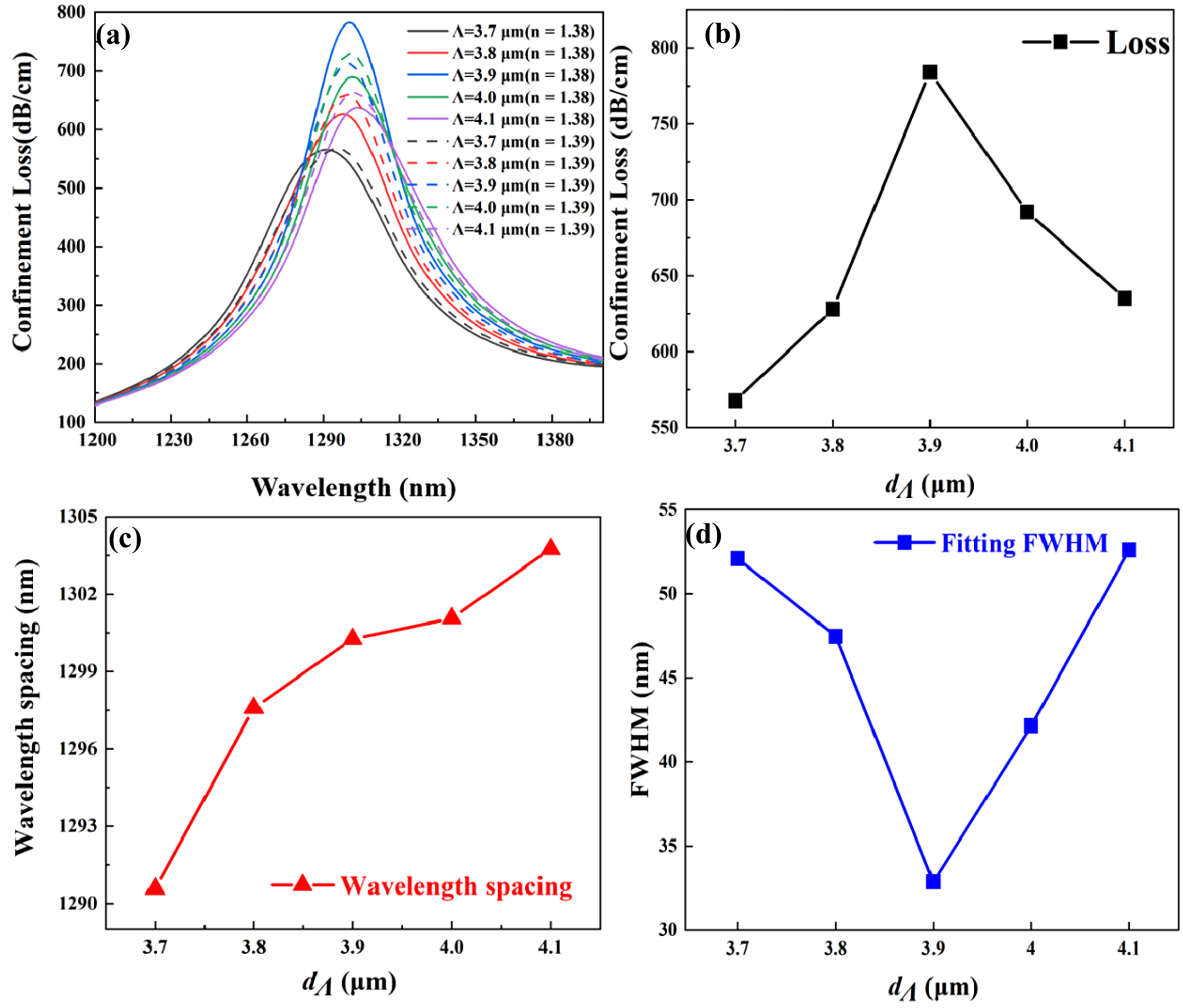


Fig. 5. (a) Influence of Λ on the loss spectrum; (b) peak total loss variation of the sensor when the Λ range is 3.6–4.2 μm; (c) variation of the resonance wavelength of the sensor when Λ ranges from 3.6 to 4.2 μm; (d) when the range of Λ is 3.6–4.2 μm, the FWHM of the sensor varies.

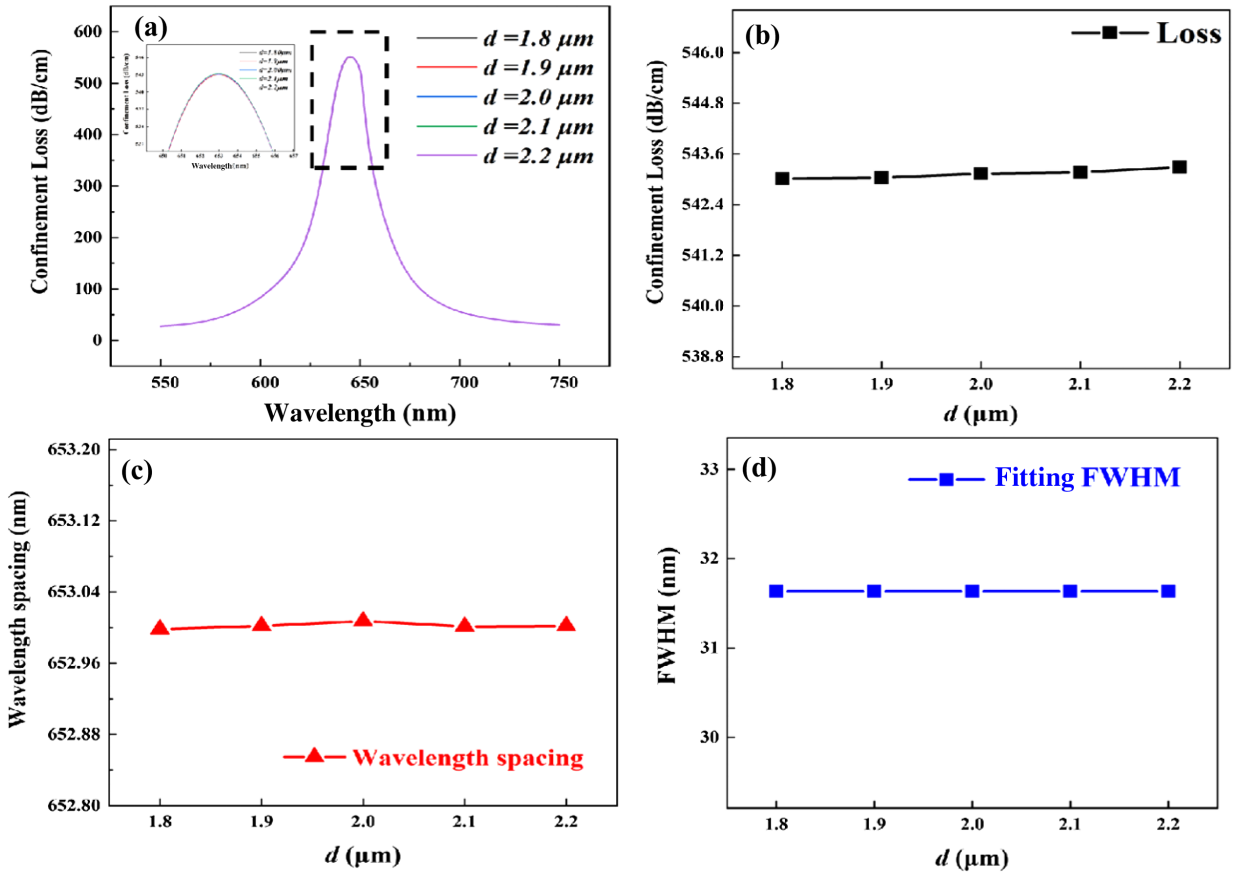


Fig. 6. (a) Influence of d on the loss spectrum; (b) peak total loss variation of the sensor when the d range is 1.8–2.2 μm; (c) variation of the resonance wavelength of the sensor when d ranges from 1.8 to 2.2 μm; (d) FWHM variation of the sensor when d ranges from 1.8 to 2.2 μm.

layer thickness is 33 nm, while the FWHM value is the smallest, which enables this sensor to improve the detection accuracy in the sensing process. Therefore, setting the gold layer thickness to 33 nm is the best solution.

5. EFFECT OF SENSING

A. Refractive Index Sensing

In this paper, the sensing performance of the optimized sensor is tested in the RI of the object to be measured in the range of 1.34–1.43.

In an SPR sensor, a change in the RI of the analyte causes a change in the SPP mode, causing a change in the wavelength at which resonance occurs. The sensitivity of the sensor is described by the ratio of the RW to the refractive index of the analyte, which can be shown by the following equation [24]:

$$S_\lambda = \frac{\Delta\lambda_{\text{peak}}}{\Delta n_a}, \tag{5}$$

where $\Delta\lambda_{\text{peak}}$ denotes the change between two adjacent RWs. Δn_a denotes the change in the RI of the analyte.

The sensor performance was further analyzed using the amplitude interrogation method, which eliminates the complexity of wavelength interpolation in the wavelength interrogation method. It can therefore be expressed as

$$S_A(\lambda) = -\frac{1}{\alpha(\lambda, n_a)} \frac{\partial\alpha(\lambda, n_a)}{\partial n_a}, \tag{6}$$

where $\alpha(\lambda, n_a)$ is the overall loss, $\partial\alpha(\lambda, n_a)$ is the difference between two consecutive loss spectra, and ∂n_a is the required change in analyte RI.

The sensor resolution (SR) of a sensor can be analyzed in terms of the sensor's ability to reveal subtle changes in RI. Subtle changes in RI can be analyzed. The calculation formula is as follows [25]:

$$\text{SR} = \partial n \times \frac{\partial\lambda_{\min}}{\partial\lambda_{\text{peak}}}, \tag{7}$$

where $\partial\lambda_{\min}$ denotes the minimum spectral resolution, $\partial\lambda_{\text{peak}}$ denotes the maximum displacement of the resonance peak, and ∂n denotes the change in two successive refractive indices. Here it is $\partial\lambda_{\min} = 0.1$ nm and $\partial n = 0.01$. The obtained SR for individual RI is shown in Table 3. The X-Pol has a peak SR of 8.7×10^{-6} RIU, which corresponds to an RI value of 1.42. Thus, the proposed sensor is qualified to detect changes in the RI of the analyte in the range of 10^{-6}.

The figure of merit (FOM) is checking the sensor detection ability of the key parameters. The calculation for the ratio of wavelength sensitivity and FWHM. The FWHM is referred to as the full-wave half-maximum. It is assumed that a higher FOM value indicates that the sensor has a better detection limit.

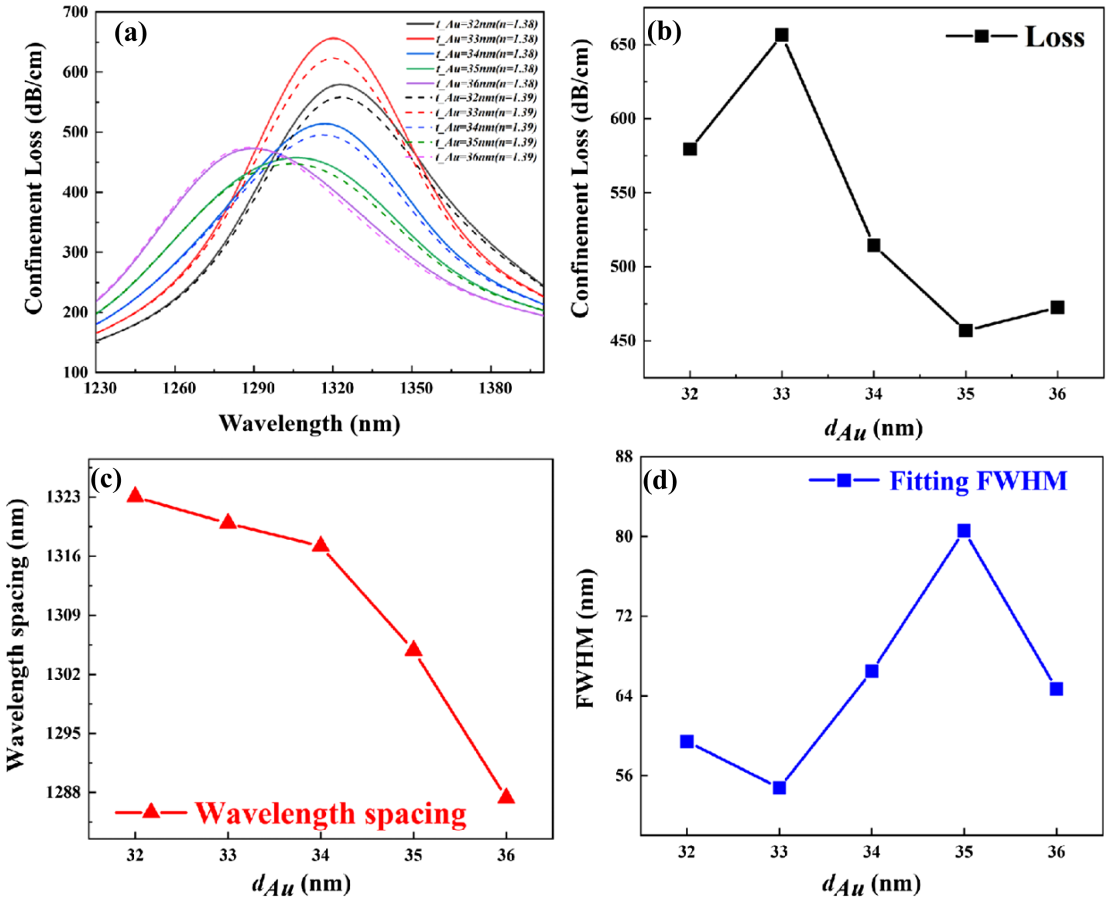


Fig. 7. (a) Influence of $t_{_Au}$ on the loss spectrum; (b) peak total loss variation of the sensor when the $t_{_Au}$ range is 32–36 nm; (c) variation of the resonance wavelength of the sensor when $t_{_Au}$ ranges from 32 to 36 nm; (d) FWHM variation of the sensor when $t_{_Au}$ ranges from 32 to 36 nm.

Table 3. Sensing Performance Analysis of Sensors by Varying the Analyte RI

Analyte (n_a)	Peak Loss (dB/cm)	λ_{peak} (nm)	$\Delta\lambda_{peak}$ (nm)	S_λ (nm/RIU)	R (RIU)	S_A (RIU^{-1})	FWHM (nm)	FOM RIU^{-1}
1.34	228.777	576	10	1000	1×10^{-4}	40.24	37.9477	26.35
1.35	257.427	586	14	1400	7.1×10^{-5}	71.08	36.1125	38.77
1.36	387.733	600	19	1900	5.3×10^{-5}	129.94	37.9482	50.07
1.37	715.831	619	22	2200	4.5×10^{-5}	349.80	16.1150	136.52
1.38	504.668	641	38	3800	2.6×10^{-5}	373.29	28.9328	133.11
1.39	494.482	679	40	4000	2.5×10^{-5}	419.98	28.5478	140.12
1.40	386.884	719	52	5200	1.9×10^{-5}	465.25	33.8521	153.61
1.41	277.801	771	72	7200	1.4×10^{-5}	465.53	55.5244	129.67
1.42	262.097	843	120	12044	8.7×10^{-6}	754.88	76.8371	149.67
1.43	268.463	963	—	—	—	—	175.1884	—

The highest FOM is derived from the maximum wavelength sensitivity and the minimum FWHM. The maximum FOM of the sensor is 153.61 RIU^{-1}.

In Table 3, the sensing characteristics of the sensor are shown for refractive indices ranging from 1.34 to 1.43. In addition, from Fig. 8(a), it can be observed that the peak of the SPR is red-shifted with increasing RI, and the RW is red-shifted from 579.89 to 958.00 nm when the RI is in the range of 1.34–1.43. The RI sensitivity reaches a maximum of 12043.8 nm/RIU. We can also find that the variation of RW is nonlinear between the same amount of refractive index changes. The main reason for this is the nonlinear dispersion change of the SPP modes leading to the nonlinear change of the resonance wavelength. $R^2 = 0.99104$ can be derived from Figs. 8(b) and 8(c). In addition, the amplitude sensitivity at different RI ranges is calculated in this paper, and it can be easily concluded that the optimum amplitude sensitivity is 754.88 RIU^{-1}.

B. Magnetic Field Sensing

The magnetic field sensing of the designed sensor is an important application of this paper, so the magnetic fluid is selectively

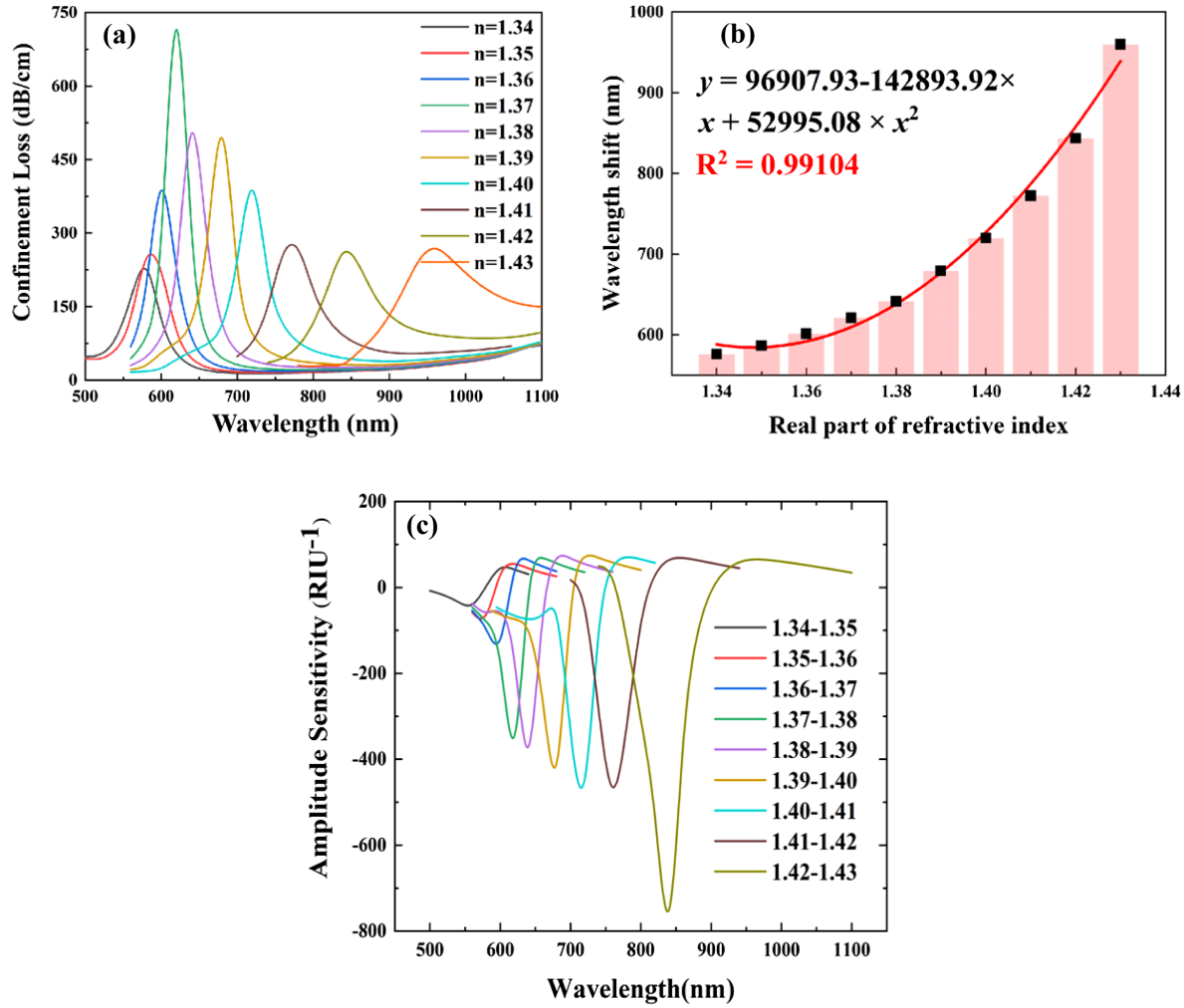


Fig. 8. (a) Influence of different RI on the loss spectrum of the optimized optical fiber sensor at the RI of 1.34–1.43; (b) fitting results of SPR resonance wavelength variation with RI of the X-Pol core mode; (c) effect of different RI on amplitude sensitivity at RI of 1.34–1.43.

filled in the elliptical channel of the two sensors to detect the magnetic field sensing effect.

To explore the characteristics of the magnetic field, the first thing to be the magnetic field sensitivity can be expressed as

$$S(H) = \frac{\Delta\lambda_{\text{peak}}}{\Delta H}, \tag{8}$$

where ΔH denotes the change in the external magnetic field. A Helmholtz coil energized by a DC power supply generates a magnetic field from 20 to 100 Oe. Changes in the RI of the magnetic fluid filling the fiber result in a shift in the SPR resonance wavelength, which is then detected by an OSA and a computer to achieve a good detection of the magnetic field. As shown in Figs. 9(a) and 9(b). Under wavelength interrogation conditions, the magneto-fluid RI is changed due to the increase of the external magnetic field, and the RW is red-shifted with the increase of MF, which leads to a similar increase in the effective refractive index of the X-Pol core mode. The maximum MF sensitivity of the sensor is 0.739 nm/Oe in the range of 20–100 Oe. This allows the proposed sensor to cope with multi-parametric measurements of magnetic field and refractive index. This significantly broadens the application area and reduces the cost.

Some recent magnetic field and refractive index sensing performances of optical fiber magnetic field sensors based on the magnetic folding effect are shown in Table 4, and it is easy to see that the magnetic field sensitivity of our optical fiber sensor is higher than most of the previous related works. The sensor has good magnetic field sensing performance in addition to maintaining good refractive index sensing performance.

6. CONCLUSION

Finally, we designed an elliptical-channel PCF-SPR sensor based on the magneto-refractive effect and investigated its magnetic field sensing by using the FVFEM. We focus on the field characteristics of the X-Pol core mode to demonstrate its magnetic field and refractive index sensing properties. Then, we also discuss the effects of gold thickness, size of air holes, and air hole spacing on the sensing performance. The max wavelength sensitivity of the designed sensor can reach 12043.8 nm/RIU, amplitude sensitivity can be achieved at 754.88 RIU^{-1}, and the magnetic field sensitivity is as high as 0.739 nm/Oe. The designed sensor maintains high refractive index sensitivity while ensuring excellent magnetic field sensing of the sensor. Due to

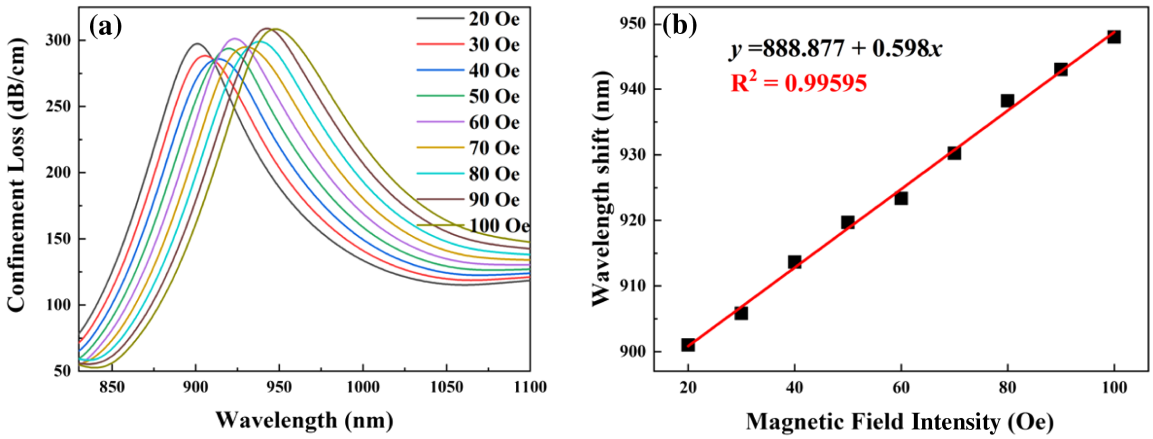


Fig. 9. (a) Effect of optimized elliptical channel fiber optic sensors on loss spectra in different magnetic fields from 20 to 100 Oe; (b) results of fitting the SPR resonance wavelength of the X-Pol core mode to the magnetic field variations in the two structures.

Table 4. Comparison of Properties of Optical Fiber Magnetic Field Sensor Reported in the Other References

Reference	Structure	S_λ (nm/RIU)	$S_{(MF)}$ (nm/Oe)	Year
[26]	PM-PCF	—	0.0242 nm/Oe	2011
[27]	Cascade: SMS	—	0.0659 nm/Oe	2015
[28]	PS-FBG	—	0.00242 nm/Oe	2018
[29]	PCF and MMF	3223 nm/RIU	0.44 nm/Oe	2021
[30]	PCF-SPR	3000 nm/RIU	0.67 nm/Oe	2022
[31]	MFS-PCF	10000 nm/RIU	0.16 nm/Oe	2022
This work	Elliptical PCF-SPR	12044 nm/RIU	0.739 nm/Oe	

its excellent sensing characteristics and simple structure, the sensor has promising applications in complex electromagnetic environments.

Funding. Heilongjiang Province Natural Science Foundation of China (ZD2023E006); Harbin Manufacturing Science and Technology Innovation Talent Project (2022CXRCCG003); Project to Enlist Young Scientific and Technological Talents in Heilongjiang Province (2022QNTJ004); Outstanding Master's and Doctor's Degree Thesis of Longjiang in New Age (LJYXL2022-064).

Disclosures. The authors declare that they have no known competing financial interests or personal relationships that could have appeared to influence the work reported in this paper.

Data availability. Data underlying the results presented in this paper are not publicly available at this time but may be obtained from the authors upon reasonable request.

REFERENCES

1. D. Wang, Y. Yu, Z. Lu, *et al.*, "Design of photonic crystal fiber to excite surface plasmon resonance for highly sensitive magnetic field sensing," Opt. Express **30**, 29271–29286 (2022).
2. F. Shao, S. Li, L. Lu, *et al.*, "High sensitivity and dual parameters micro-tapered-LPG sensor," Opt. Lasers Eng. **164**, 107498 (2023).
3. H. Nakamura, Y. Mizuno, and S. E. Pandarakone, "Development of a high-performance magnetic field sensor and its application to a magnetic field visualization system using the augmented reality technique," J. Sens. **2019**, 5848514 (2019).
4. M. Cavaliere, O. McVeigh, H. Jaeger, *et al.*, "Inductive sensor design for electromagnetic tracking in image guided interventions," IEEE Sens. J. **20**, 8623–8630 (2020).
5. S. Qin, J. Lu, Y. Yu, *et al.*, "Magnetic field and temperature two-parameter sensor based on optical microfiber coupler interference (OMCI) wrapped with magnetic fluid and PDMS," Opt. Express **29**, 29492–29504 (2021).
6. S. Gu, W. Sun, M. Li, *et al.*, "Simultaneous measurement of magnetic field and temperature based on photonic crystal fiber plasmonic sensor with dual-Polarized modes," Optik **259**, 169030 (2022).
7. O. Oehlsen, S. I. Cervantes-Ramírez, P. Cervantes-Avilés, *et al.*, "Approaches on ferrofluid synthesis and applications: current status and future perspectives," ACS Omega **7**, 3134–3150 (2022).
8. S. Liu, B. Yu, S. Wang, *et al.*, "Preparation, surface functionalization and application of Fe_3O_4 magnetic nanoparticles," Adv. Colloid Interface Sci. **281**, 102165 (2020).
9. D. Wang, Z. Yi, G. Ma, *et al.*, "Two-channel photonic crystal fiber based on surface plasmon resonance for magnetic field and temperature dual-parameter sensing," Phys. Chem. Chem. Phys. **24**, 21233–21241 (2022).
10. D. Wang, W. Zhu, Z. Yi, *et al.*, "Highly sensitive sensing of a magnetic field and temperature based on two open ring channels SPR-PCF," Opt. Express **30**, 39055–39067 (2022).
11. D. Xie, H. Zhang, G. Wang, *et al.*, "Sensitivity and linearity enhanced wide-detection range surface-plasmon-resonance photonic-crystal-fiber sensor," Results Phys. **29**, 104707 (2021).
12. R. Hao, D. Li, W. Yang, *et al.*, "Study on magnetic model and magnetic force of magnetic fluid in pressure difference sensor," Adv. Mater. Res. **779**–780, 282–285 (2013).
13. Y. Zhao, R. Lv, Y. Zhang, *et al.*, "Novel optical devices based on the transmission properties of magnetic fluid and their characteristics," Opt. Lasers Eng. **50**, 1177–1184 (2012).
14. R. Q. Lv, H. Li, and H.-F. Hu, "Theoretical analysis and experimental measurement of birefringence properties in magnetic fluid subjected to magnetic field," IEEE Trans. Magn. **51**, 6600105 (2015).
15. H. Liu, C. Chen, H. Wang, *et al.*, "Simultaneous measurement of magnetic field and temperature based on surface plasmon resonance in twin-core photonic crystal fiber," Optik **203**, 164007 (2020).
16. G. Wang, Y. Lu, X. Yang, *et al.*, "High-sensitivity magnetic field sensor based on a dual-core photonic crystal fiber," Appl. Opt. **58**, 5800–5806 (2019).

17. M. Wang, Y. Lu, C. Hao, *et al.*, "Simulation analysis of a temperature sensor based on photonic crystal fiber filled with different shapes of nanowires," Optik **126**, 3687–3691 (2015).
18. S. Singh and Y. K. Prajapati, "TiO_2/gold-graphene hybrid solid core SPR based PCF RI sensor for sensitivity enhancement," Optik **224**, 165525 (2020).
19. Y.-T. Chen, S.-Y. Yang, W. S. Tse, *et al.*, "Thermal effect on the field-dependent refractive index of the magnetic fluid film," Appl. Phys. Lett. **82**, 3481–3483 (2003).
20. W. Liu, Y. Shi, Z. Yi, *et al.*, "A surface plasmon resonance chemical sensor composed of microstructured optical fibers for detection of an ultra-wide refractive index range and gas-liquid Pollutants," Opt. Express **29**, 40734–40747 (2021).
21. M. M. Rahman, M. A. Molla, A. K. Paul, *et al.*, "Numerical investigation of a highly sensitive plasmonic refractive index sensor utilizing hexagonal lattice of photonic crystal fiber," Results Phys. **18**, 103313 (2020).
22. M. Islam, M. Islam, J. Sultana, *et al.*, "Exposed core localized surface plasmon resonance biosensor," J. Opt. Soc. Am. B **36**, 2306–2311 (2019).
23. S. Yao, Y. Yu, S. Qin, *et al.*, "Research on optimization of magnetic field sensing characteristics of PCF sensor based on SPR," Opt. Express **30**, 16405–16418 (2022).
24. A. Zuhayer, M. Abd-Elnaby, S. H. Ahammad, *et al.*, "A gold-plated twin core d-formed photonic crystal fiber (PCF) for ultrahigh sensitive applications based on surface plasmon resonance (SPR) approach," Plasmonics **17**, 2089–2101 (2022).
25. T. Wang, M. Zhang, K. Liu, *et al.*, "The effect of the TiO_2 film on the performance of the optical fiber SPR sensor," Opt. Commun. **448**, 93–97 (2019).
26. S. A. Mitu, D. K. Dey, K. Ahmed, *et al.*, "Fe_3O_4 nanofluid injected photonic crystal fiber for magnetic field sensing applications," J. Magn. Magn. Mater. **494**, 165831 (2020).
27. L. Luo, S. Pu, S. Dong, *et al.*, "Fiber-optic magnetic field sensor using magnetic fluid as the cladding," Sens. Actuators A Phys. **236**, 67–72 (2015).
28. L. Bao, X. Dong, S. Zhang, *et al.*, "Magnetic field sensor based on magnetic fluid-infiltrated phase-shifted fiber Bragg grating," IEEE Sens. J. **18**, 4008–4012 (2018).
29. L. Zhu, N. Zhao, Q. Lin, *et al.*, "Optical fiber SPR magnetic field sensor based on photonic crystal fiber with the magnetic fluid as cladding," Meas. Sci. Technol. **32**, 075106 (2021).
30. I. Danlard, I. O. Mensah, and E. K. Akowuah, "Design and numerical analysis of a fractal cladding PCF-based plasmonic sensor for refractive index, temperature, and magnetic field," Optik **258**, 168893 (2022).
31. M. Islam, M. M. I. Khan, A. Al Naser, *et al.*, "Design of a quad channel SPR-based PCF sensor for analyte, strain, temperature, and magnetic field strength sensing," Opt. Quantum Electron. **54**, 563 (2022).